Acta Materialia 118 (2016) 152–163

Contents lists available at ScienceDirect

Acta Materialia

journal homepage: www.elsevier.com/locate/actamat

Full length article

Microstructure evolution and critical stress for twinning in the CrMnFeCoNi high-entropy alloy

G. Laplanche*, A. Kostka, O.M. Horst, G. Eggeler, E.P. George

Institut für Werkstoffe, Ruhr-Universität Bochum, D-44801 Bochum, Germany

ARTICLE INFO

Article history:
Received 24 June 2016
Received in revised form
18 July 2016
Accepted 20 July 2016
Available online 31 July 2016

Keywords:
CoCrFeMnNi high-entropy alloy
Strain hardening
Transmission electron microscopy (TEM)
Dislocation density
Deformation twinning

ABSTRACT

At low homologous temperatures (down to cryogenic temperatures), the CrMnFeCoNi high-entropy alloy possesses good combination of strength, work hardening rate (WHR), ductility, and fracture toughness. To improve understanding of the deformation mechanisms responsible for its mechanical properties, tensile tests were performed at liquid nitrogen and room temperature (77 K and 293 K) and interrupted at different strains to quantify the evolution of microstructure by transmission electron microscopy. Dislocation densities, and twin widths, their spacings, and volume fractions were determined. Nanotwins were first observed after true strains of ~7.4% at 77 K and ~25% at 293 K; at lower strains, deformation occurs by dislocation plasticity. The tensile stress at which twinning occurs is 720 ± 30 MPa, roughly independent of temperature, from which we deduce a critical resolved shear stress for twinning of 235 ± 10 MPa. In the regime where deformation occurs by dislocation plasticity, the shear modulus normalized WHR decreases with increasing strain at both 77 K and 293 K. Beyond ~7.4% true strain, the WHR at 77 K remains constant at a high value of $G/30$ because twinning is activated, which progressively introduces new interfaces in the microstructure. In contrast, the WHR at room temperature continues to decrease with increasing strain because twinning is not activated until much later (close to fracture). Thus, the enhanced strength-ductility combination at 77 K compared to 293 K is primarily due to twinning starting earlier in the deformation process and providing additional work hardening. Consistent with this, when tensile specimens were pre-strained at 77 K to introduce nanotwins, and subsequently tested at 293 K, flow stress and ductility both increased compared to specimens that were not pre-strained.

1. Introduction

The equiatomic high-entropy alloy (HEA), CrMnFeCoNi, is one of the most thoroughly studied HEAs from both experimental and theoretical points of view, e.g., [1–30]. Here we focus on its mechanical properties, which are quite interesting, as has been summarized recently in two review papers [24,31]. In particular, Gali and George [3] first showed that the yield strength, ultimate tensile strength and ductility of the CrMnFeCoNi HEA all increase simultaneously when the temperature is lowered from 293 K to 77 K. Furthermore, it exhibits very high fracture toughness down to 77 K [13]. These mechanical properties run counter to the usual inverse relationship between strength and toughness/ductility. Otto et al. [4] concluded using transmission electron microscopy (TEM) that the increase in ductility with decreasing temperature is related to the occurrence of two deformation mechanisms at 77 K, namely, dislocation glide and mechanical twinning; in contrast, they observed only dislocation glide at 293 K. Similar reasoning was employed by Gludovatz et al. [13] to explain the high fracture toughness at cryogenic temperatures. Otto et al. [4] attributed twinning to the low stacking fault energy of the CrMnFeCoNi HEA, which has been reported to be about 20–25 mJ/m^2 [7,19].

Despite these findings, there are major limitations in our mechanistic understanding of plasticity in this HEA that stem from the fact that Otto et al. [4] performed TEM analysis after just two engineering strains, approximately 2% and 20%. Therefore, their study left several important questions unanswered, including the following: (1) when exactly does twinning start at 77 K? Otto et al. [4] showed that there were no twins after 2% strain, but twins were present after 20% strain, which left a large unexplored gap in between. (2) Does twinning occur at room temperature in uniaxial tension? This is important because twinning has been observed at

* Corresponding author.
E-mail address: guillaume.laplanche@rub.de (G. Laplanche).

http://dx.doi.org/10.1016/j.actamat.2016.07.038

room temperature under different stress states (high pressure torsion [22], rolling [30], and *in situ* straining of thin films in the TEM [23]). Perhaps the reason Otto et al. [4] did not find twins after room-temperature deformation was because they did not examine specimens that were deformed heavily enough (>20% strain). (3) Is there a critical stress for twinning? If so, does it depend on temperature? (4) How does the onset of mechanical twinning affect flow stress and work hardening rate (WHR)? (5) Is the higher WHR at 77 K primarily related to twinning? (6) How does dislocation density increase with strain, and is there a difference between its evolution at 77 K and 293 K? (7) What is the dependence of flow stress on dislocation density at the two temperatures? To answer these outstanding questions, we use TEM to assess the evolution of dislocation density, volume fraction of twins, twin width, and twin spacing in specimens strained to several different levels at 77 K and 293 K.

2. Experimental methods

2.1. Processing

Starting with elemental metals (>99.9% pure), an ingot of the equiatomic CrMnFeCoNi HEA measuring 40 mm in diameter and 120 mm in length was produced by vacuum induction melting and casting as described elsewhere [21]. After homogenization at 1473 K for 48 h, the alloy was rotary swaged at room temperature to produce a rod with a diameter of 16.5 mm, which was then recrystallized at 1173 K for 1 h. It has been shown previously that the above deformation processing and heat treatment steps result in a homogeneous microstructure with almost no texture and a mean grain size of 17 μm [21]. Additionally, chemical analysis of a similarly processed alloy yielded carbon, oxygen, and sulfur levels of 0.051, 0.032, and 0.009 at.%, respectively, and concentrations of the primary constituents of 19.41 Cr, 20.10 Mn, 20.55 Fe, 20.26 Co and 19.58 Ni (at.%) [20]. Consequently, we assume that the alloy investigated here is close to the equiatomic composition, CrMnFeCoNi, with relatively low levels of impurities.

2.2. Mechanical testing

Rectangular dog-bone shaped tensile specimens with gauge lengths of 20 mm were machined from the recrystallized material by electrical discharge machining. The loading direction was parallel to the cylindrical axis of the swaged rod. Both sides of the specimen were ground to 1000 grit finish using SiC paper resulting in a final thickness of ~1.2 mm and a gauge section of ~4.8 mm^2 containing more than 20000 grains. Tensile tests were performed at an engineering strain rate of 10^{-3} s^{-1} in a screw-driven Zwick/Roell test rig of type Z100 at liquid nitrogen temperature (77 K) and room temperature (293 K). Two different methods were adopted for determining the engineering strains. Tests performed at room temperature employed an extensometer directly attached to the gauge section that measured displacements. The extensometer could not be used at liquid nitrogen temperature, so strains had to be determined indirectly from the crosshead displacement. The displacement of the crosshead is typically larger than the real displacement in the gauge section (because of deformation in the shoulders of the tensile specimen, load-train, etc.), so a correction factor has to be used. In this study, we determined the difference between the extensometer and crosshead displacements at room temperature and assumed the same difference at 77 K for use as the correction factor. The engineering strains thus determined were used to calculate true stress-strain curves assuming constancy of volume during plastic deformation. Our stress-strain curves are in good agreement with those reported in the literature for this HEA [4,32]. Additionally, we measured the elongations of specimens after fracture using a light microscope and they showed good agreement with the elongations obtained from the crosshead displacements that were corrected as described above.

2.3. Transmission electron microscopy (TEM)

Several microstructural characterization techniques have been used in the literature to determine the volume fractions of twins, distributions of twin widths, and their mean spacing: optical microscopy [33,34], electron backscatter diffraction (EBSD) [35], electron channeling contrast imaging (ECCI) [36,37], and TEM [38]. As the mechanical twins in the CrMnFeCoNi HEA were reported to have widths of just a few nanometers [4], a high-resolution technique is needed to determine the spacing between twins. Therefore, in the present study, we used TEM and covered an area of at least 2500 μm^2 (~10 grains) in each specimen to obtain reasonable statistics. In addition to the quantitative assessment of mechanical twinning, dislocation densities were systematically evaluated after deformation using Ham's method [39]. A grid was used to determine the number of dislocations intersected per unit length of grid lines, N_d. The dislocation density ρ can then be calculated using $\rho = 2\ N_d\ /\ t_f$, where t_f is the thickness of the TEM foil. These thicknesses were determined for each dislocation density measurement (4 areas in each material state) using the Kossel fringe technique [40–42] with diffraction vectors $\boldsymbol{g}$ of type 111. The foil thicknesses ranged from 150 nm (heavily deformed specimens) to 460 nm (undeformed specimens and specimens with small accumulated strains).

For both the twin and dislocation density measurements, tensile tests were interrupted after different strains and slices were cut from their gauge sections and ground to a thickness of 90 μm using 600-grit SiC paper. Subsequently, TEM foils were prepared using double-jet electrochemical thinning at 20 V in an electrolyte consisting of 70 vol% methanol, 20 vol% glycerine and 10 vol% perchloric acid at 253 K. TEM analyses were performed on a Tecnai Supertwin F20 G2 instrument operating at 200 kV.

2.4. Quantitative evaluation of mechanical twinning

The evolution of mechanical twinning with strain was characterized as follows. To measure their widths (thickness), the TEM specimen was tilted to observe the deformation twins edge-on and their widths were then directly measured (measurements were performed in at least 5 grains of each specimen). The mean twin spacing was determined using a grid placed on a montage created from several low magnification TEM images as shown in Fig. 1. To create the montage, individual grains were tilted to make all their nanotwins visible (in general, the diffraction conditions required for such imaging differ from grain to grain). The specimen tilts were always less than 10° which yield a maximum underestimation of the mean twin spacing of less than 2%. This can be neglected relative to the magnitudes of the experimental uncertainties (see error bars for the mean twin spacings in the Results and Discussion section). Two regions of the montage are magnified on the right side of Fig. 1. Some regions, such as the one in the lower right corner of Fig. 1, are devoid of mechanical twins and exhibit only dislocations. In contrast, in the upper right corner, the intersections of two white lines of the grid with nanotwins are highlighted with white circles as examples to show how the number of twins N intersected per unit length of the grid lines can be determined. The mean spacing λ between twins can then be calculated using $N = 1/\lambda$ [33]. When bundles of nanotwins were encountered, they were treated as follows for the assessment of the parameters N and λ. In polycrystals, the well-known Hall-Petch relationship is found to hold

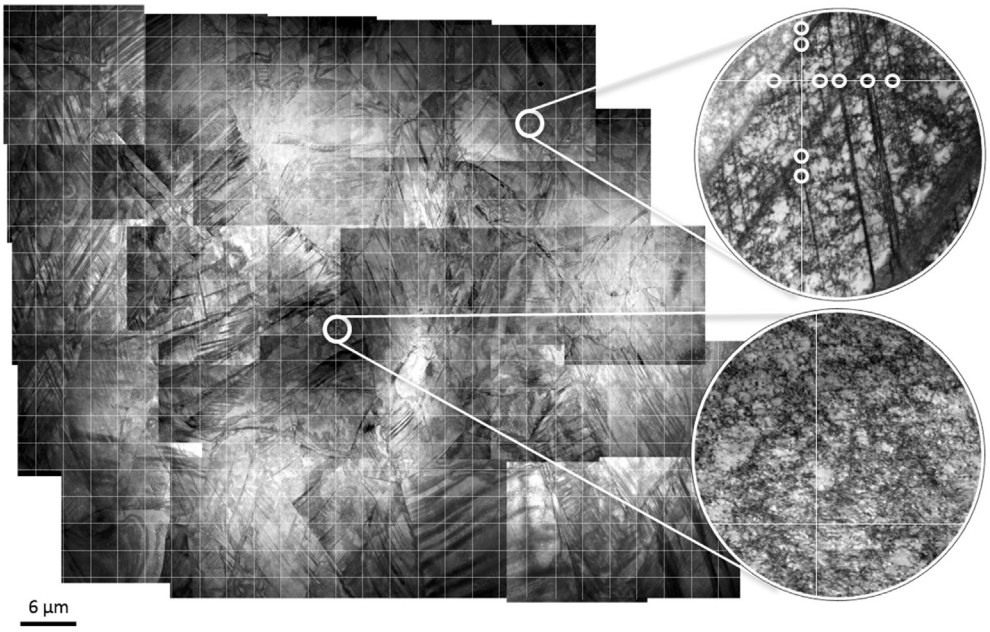

Fig. 1. Representative montage of TEM bright field images covering an area of about 4000 μm^2 with a superimposed grid pattern to illustrate our procedure for the evaluation of mean twin spacing.

for grain sizes larger than about 1 μm [43,44]. However for submicrometer grain sizes in the nanocrystalline regime, a deviation from the Hall-Petch trend has been observed. Following the convention in the nanocrystalline literature [43], twin spacings smaller than 25 nm (cut-off value) were not counted in the present study, i.e. if a bundle contains multiple twins that are thinner than 25 nm, we consider the total thickness of the bundle instead of the width of the individual nanotwins, and if such a bundle is intersected by a grid line, that intersection is counted as one intersection.

3. Results and discussion

3.1. Tensile properties

Representative engineering stress-strain curves of the CrMnFeCoNi HEA tensile tested to fracture at 77 K and 293 K are shown in Fig. 2a and the corresponding true stress-strain curves are shown in Fig. 2b. The increase in strength and ductility at lower temperature is reminiscent of earlier reports [3,4,13,32]. Based on an average of 10 tests at each temperature, our current results show that the engineering yield strength σ_y increases from 265 ± 10 MPa to 460 ± 30 MPa and the ultimate tensile strength σ_{uts} increases from 600 ± 40 MPa to 1060 ± 70 MPa when the temperature decreases from 293 K to 77 K. Along with the strength increase, the tensile ductility (strain to failure) also increases by ~50% when the temperature is decreased from room temperature to 77 K. In order to study the evolution of microstructure and, in particular, the onset of twinning during plastic deformation, tensile tests at 77 K and 293 K were interrupted at the different strain levels indicated by the arrows in Fig. 2a so that TEM specimens could be extracted from their gauge sections. In addition, specimens tested to failure at the two temperatures were also examined, as indicated by the arrows at the ends of the curves.

Fig. 2c shows the true strain hardening rate normalized by the shear modulus $(d\sigma/d\varepsilon)/G$ as a function of the true strain where G is 85 and 80 GPa at 77 K and 293 K, respectively [20,45]. Note that the thickness of the lines represents the scatter in the strain hardening rate obtained from three different tests. At 293 K, the strain hardening rate shows a monotonic decay with increasing strain. This behavior is typical for metallic alloys [36]. In contrast, the strain hardening rate at 77 K reveals distinctly different behavior with three distinguishable stages. The first stage is characterized by a continuous decrease in the strain hardening rate from ~G/20 initially to ~ G/30 at ~10% true strain, similar to that observed at 293 K. At larger strains (10–35%), a second stage appears where the strain hardening rate remains almost constant around G/30. Finally, in the third stage the strain hardening rate again decreases until rupture at ~44%. The mechanisms underlying the different trends at 77 K and 293 K will be discussed below after the differences in microstructural evolution at the two temperatures are described.

3.2. Critical stress for twinning and evolution of twins with strain

Prior to straining, the recrystallized alloy has a very low dislocation density as shown in Fig. 3; this is similar to what has been observed before [4]. However, in that earlier study [4] microstructures of deformed specimens were investigated only after relatively low and high tensile strains, approximately 2 and 20%, respectively. As a result, only limited inferences could be made about how microstructure evolves with strain. To obtain a better understanding of how the dislocation and twin densities increase with strain, and to quantify the stress at which twinning starts, here we investigate multiple material states after different levels of accumulated strain. First we discuss the evolution of twin density with strain at 77 K as summarized in Fig. 4. After 2.1% true strain (Fig. 4a), the microstructure shows an increase in dislocation density relative to the unstrained (as-recrystallized) state (Fig. 3). No deformation twins could be detected and the tensile deformation is fully accommodated by planar dislocation glide on several slip systems, see Fig. 4a, where dislocation pile-ups at grain boundaries can be seen. There is a similar absence of deformation twins after a true strain of 3.7% (third blue arrow in Fig. 2a), but a TEM image is not shown here to save space.

At a true strain of 6.0%, the first evidence was found for nanotwins (widths ~ 5–20 nm), as shown in Fig. 4b. However, only one

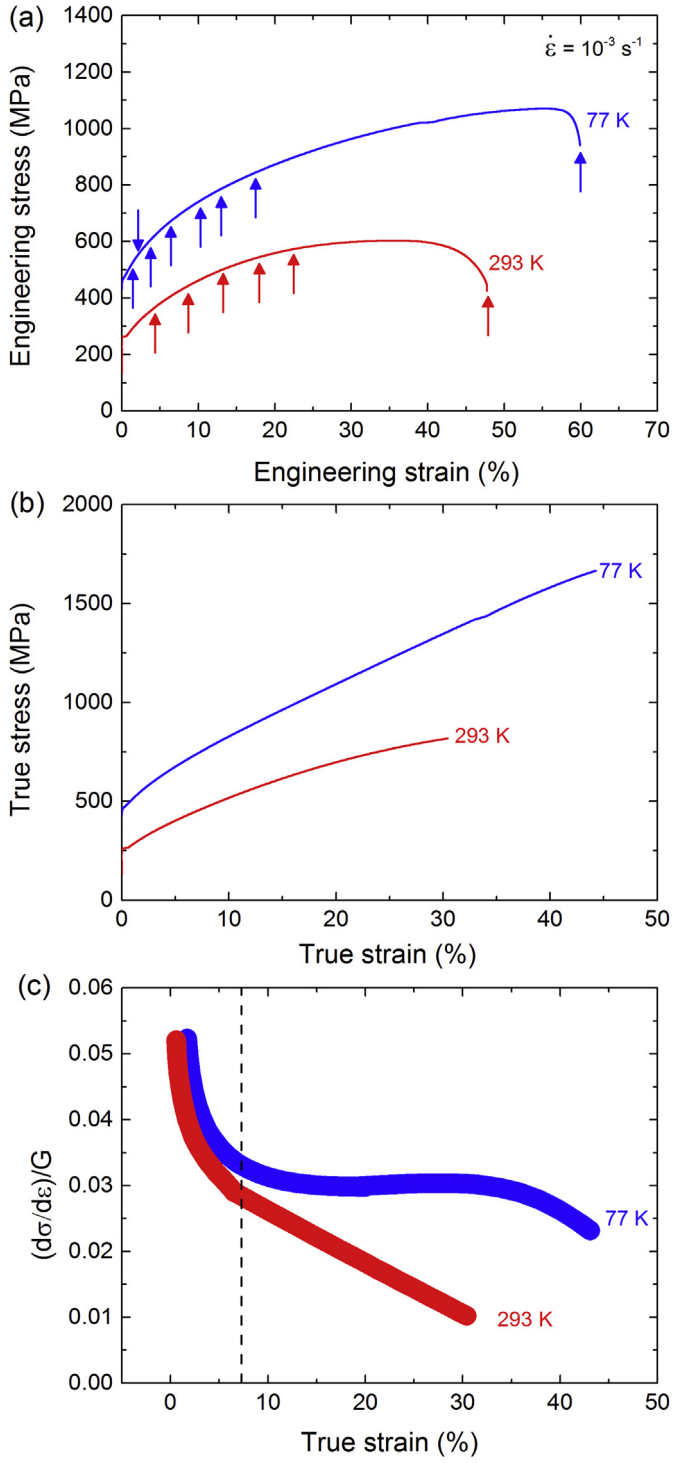

Fig. 2. Representative (a) engineering and (b) true stress-strain curves of tensile tests at 77 K and 293 K. The arrows in (a) indicate the strains at which several additional tensile tests were interrupted to study the evolution of microstructure. (c) True strain-hardening rate normalized by the shear modulus as a function of true strain.

of 20 grains examined contained nanotwins; most grains still contained only dislocations. Note that in this figure (as well as in Fig. 4c–e), the images in the left column are bright field (BF) images, those in the middle column are higher magnification dark field (DF) images, and selected area diffraction (SAD) patterns are shown in the right column. Furthermore, all the nanotwins in

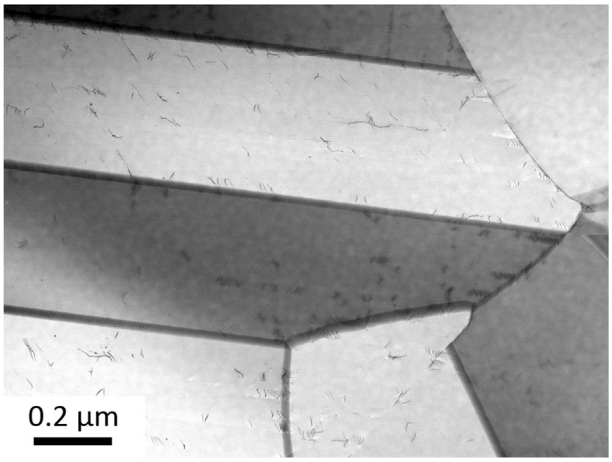

Fig. 3. TEM micrograph of the CrMnFeCoNi high-entropy alloy in the as-recrystallized state.

Fig. 4b–e are edge-on and the diffraction spots used to obtain the DF images of the nanotwins are marked with red circles in the corresponding SAD patterns. At a larger true strain (8.8%), practically all the grains contain deformation twins, as shown by the example in Fig. 4c. In other words, the first twins appear sporadically at a true strain of ~6% but when the true strain reaches ~9% they are present in almost all grains. With increasing strain, the volume fraction of twins increases systematically, as can be seen in Fig. 4c–e. Above 15% strain, several intersecting twins are present within the grains as shown on the left side of Fig. 4e; consistent with this, multiple intersecting twin systems are observed in the fractured specimen (see Fig. 1).

Based on the above observations it is reasonable to conclude that, at 77 K, the true strain at which twins can be consistently observed is between 6.0% and 8.8%; to keep it simple, we assume that it is in the middle of this range, 7.4 ± 1.4%. This corresponds to an applied true stress of 720 ± 30 MPa at 77 K, hereafter referred to as the twinning stress, σ_{tw}, as shown in Fig. 5. If this is a "critical" stress that is characteristic of a given material and grain size, then twinning should be observed also at room temperature in our HEA as long as the stress in the tensile specimens reaches this value. As discussed before, Otto et al. [4] did not observe twins after 20% engineering strain at room temperature. We hypothesized that it was because their specimen did not experience a high enough stress, and not because twinning is impossible at room temperature. As shown in Fig. 5, true strains exceeding ~20% (i.e., engineering strains exceeding 22.3%) are needed at room temperature to reach the critical twinning stress of ~720 MPa. To check whether our reasoning is correct, we examined specimens that were subjected to tensile stresses of 680 MPa and 820 MPa, which are, respectively, below and above the expected critical twinning stress of 720 ± 30 MPa. Interestingly, no twins were observed in the 680-MPa specimen, whereas they were definitely present in the 820-MPa specimen (the latter actually had to be strained to fracture to reach this high stress level). In the 820-MPa specimen, care was taken to extract the TEM specimen from a region of uniform elongation far from the necked region. Its microstructure is shown in Fig. 6 where the TEM BF image in Fig. 6a shows a bundle of mechanical twins in the vicinity of a grain boundary. As before (Fig. 4), all the twins in Fig. 6 are edge-on. The region enclosed with a dashed white rectangle is shown as a magnified DF image in Fig. 6b where the bundle of deformation twins exhibits bright contrast while the surrounding matrix is darker. The corresponding

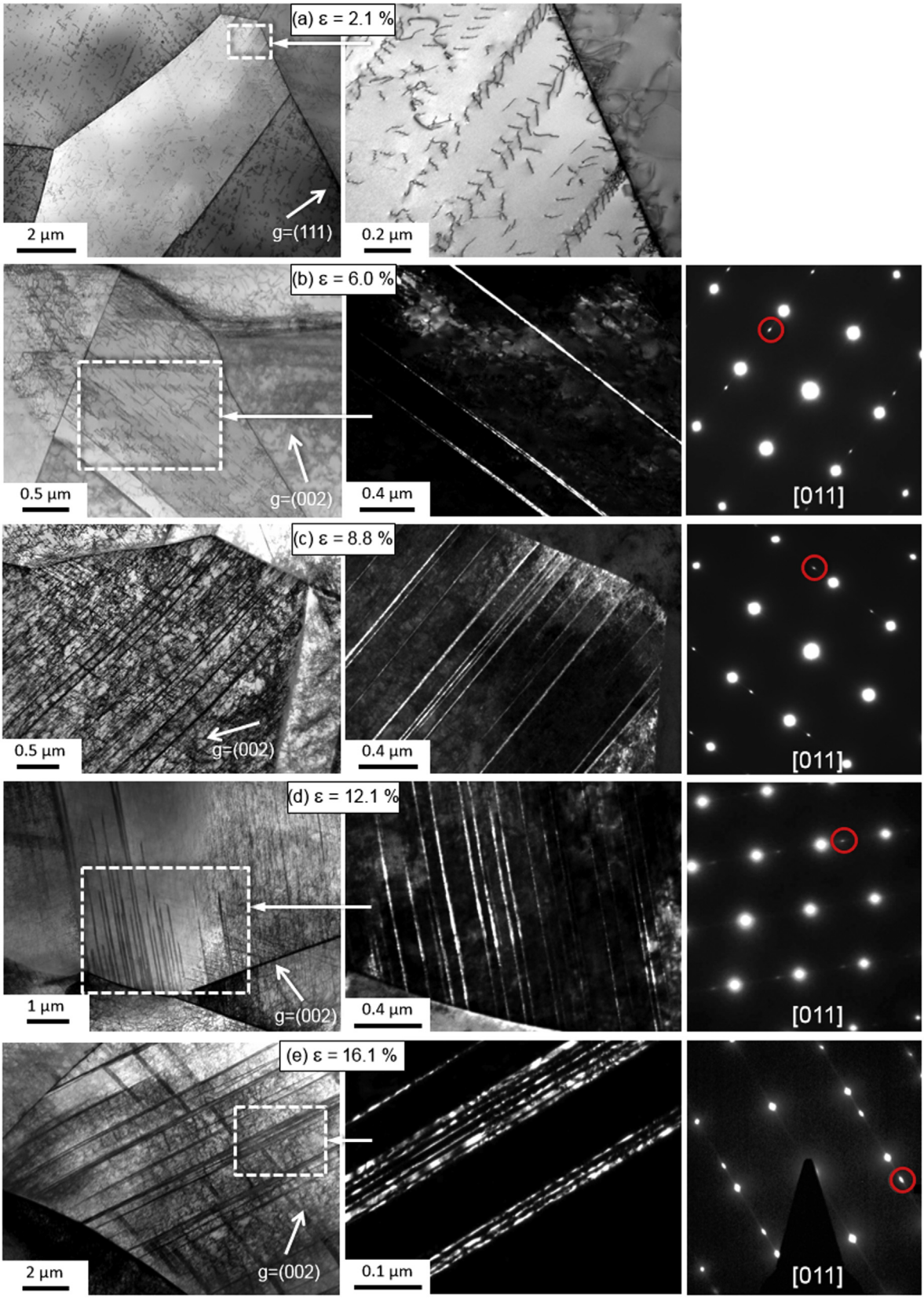

Fig. 4. TEM micrographs showing twin evolution with true tensile strain at 77 K. (a) Both figures are bright field images. (b–e) Figures on the left are bright field images while those in the middle are dark field images with SAD patterns on the right showing diffraction spots from the twin and matrix. Diffraction spots circled in red in the SAD patterns were used to obtain the dark field images. The dashed rectangles in the left column delineate areas that are magnified in the middle column. (For interpretation of the references to color in this figure legend, the reader is referred to the web version of this article.)

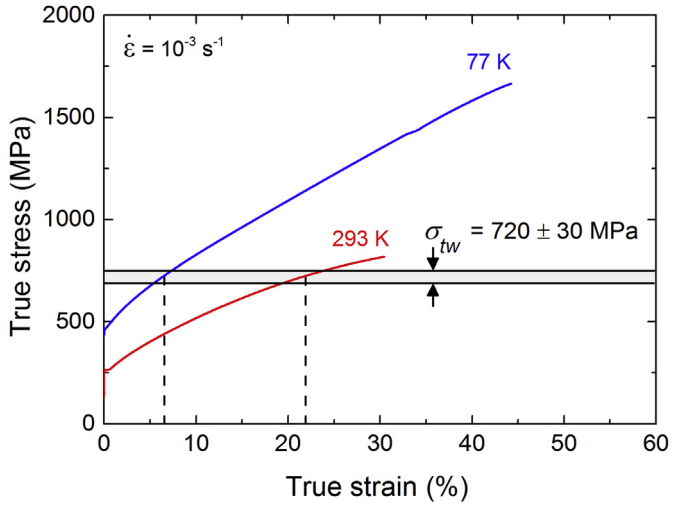

Fig. 5. True stress-strain curves with a band showing the critical stress for twinning σ_{tw} determined by TEM examination of interrupted tensile specimens.

SAD pattern (Fig. 6c) reveals two sets of diffraction spots belonging to the FCC deformation twin and the FCC matrix; the diffraction spot used for the DF image is marked with a red circle. Clearly, twinning does occur at room temperature in the CrMnFeCoNi HEA, albeit at much higher strains than at 77 K, and the reason it was not seen in the previous study [4] was that specimens strained to a high-enough level were not examined.

From the polycrystalline twinning stress of 720 ± 30 MPa, assuming a Taylor factor of 3.06, the critical resolved shear stress for twinning can be estimated as 235 ± 10 MPa. This value is higher than the value of 208 MPa [25] calculated using density functional theory and may be related to our relatively small grain size (17 μm) since it has been reported [46] that the twinning stress follows a Hall-Petch type relationship. Therefore, it is not unreasonable to suppose that the critical resolved shear stress for twinning in a material with a grain size of 17 μm is higher than that calculated by DFT for single crystals.

Distributions of twin widths determined from TEM analyses of specimens deformed to true strains of 8.8, 12.1, 16.1 and 44.2% at 77 K are shown in Fig. 7 where the average width in each case is indicated by a red dashed line. The average twin width increases slightly from 12 nm to 15 nm when the true strain increases from 8.8% to 12.1%. Above 16% strain, the twin width seems to remain constant around 32 nm. The increase in twin width is possibly related to the merging of nanotwins with increasing strain. The evolution of λ, the average distance between twins (or mean twin spacing), as a function of the applied strain is shown in Fig. 8a. Note that the error bars correspond to ±1 standard deviation of four measurements on segments of cumulative length of at least 500 μm. There is an initial rapid decrease followed by a saturation around 1.3 μm at large strains. From the data shown in Figs. 7 and 8a, the volume fraction of twins was calculated using Fullman's volumetric analysis for a distribution of thin twins [47]:

$$N = \frac{1}{\lambda} = \frac{1}{2t}\frac{f}{1-f}, \quad (1)$$

where t is the width of the twins and f is their volume fraction. The evolution of f with strain is shown in Fig. 8b (vertical axis on the left). Twinning starts after a critical strain of ~7.4% beyond which f increases almost linearly up to 0.05 at ~45% true strain.

Based on the above results, it is possible to make a rough

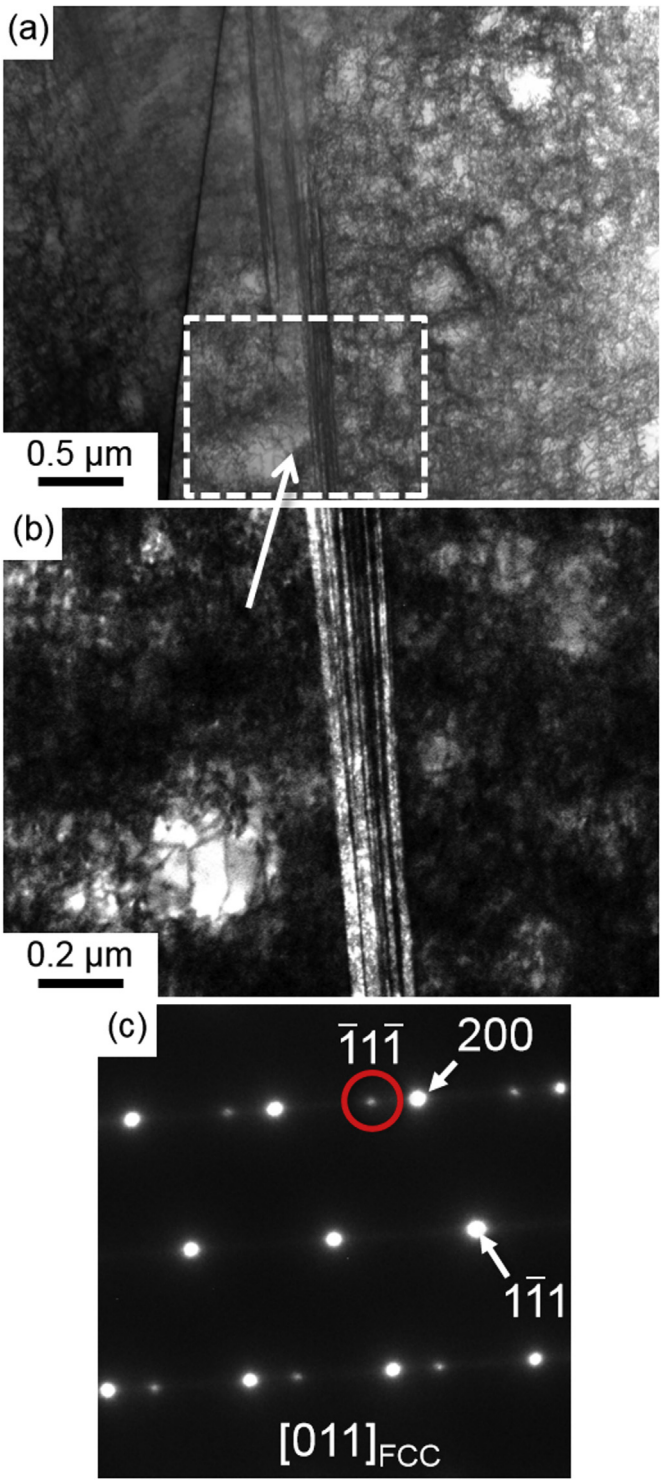

Fig. 6. TEM images of twins in a tensile specimen strained to fracture at 293 K (uniform elongation: ~30%). (a) Bright field image (b) higher magnification dark field image of dashed rectangular area in (a). (c) SAD pattern showing diffraction spots from twin and matrix. The diffraction spot circled in red in the SAD pattern was used to obtain the dark field image. (For interpretation of the references to color in this figure legend, the reader is referred to the web version of this article.)

estimate of the contribution that twins make to the overall tensile strain as follows. If the whole volume of a single crystal having the FCC structure were to twin (i.e., $f = 1$), the resulting shear strain

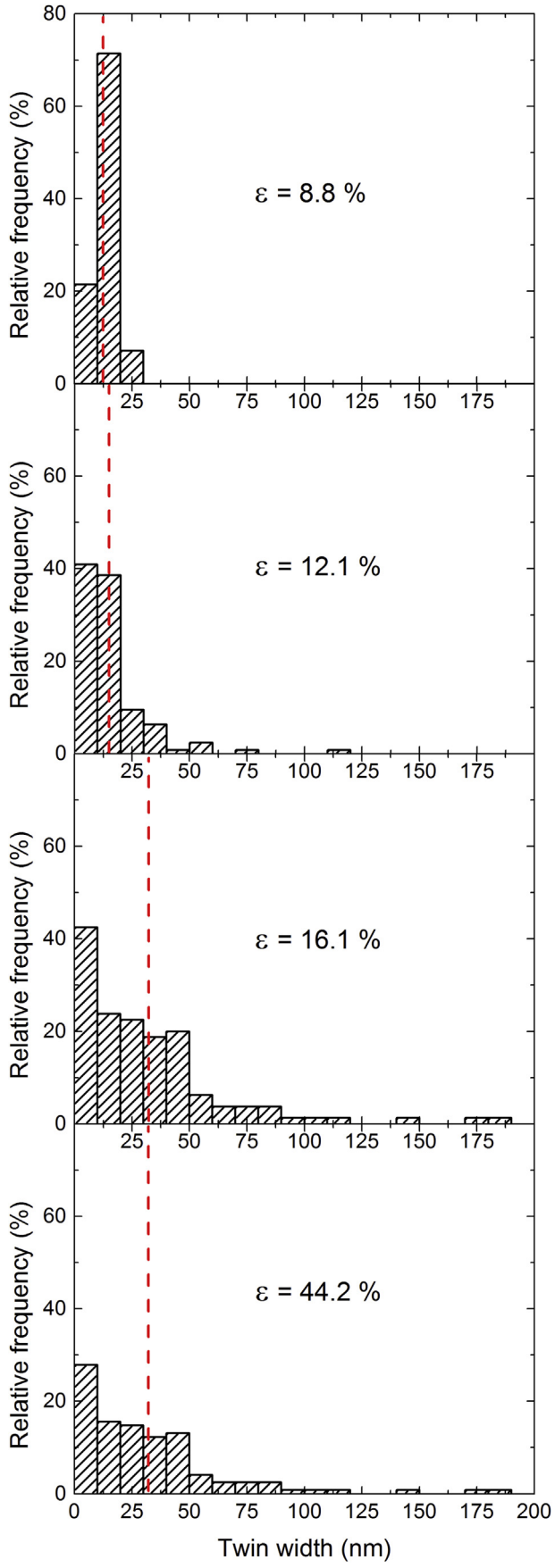

Fig. 7. Distributions of twin widths as a function of true tensile strains at 77 K. The red dashed lines indicate the average twin widths. (For interpretation of the references to color in this figure legend, the reader is referred to the web version of this article.)

would be 0.707. This can be converted to a polycrystalline tensile strain of 0.23 by taking into account the Taylor factor of 3.06. In our polycrystalline HEA, since the whole volume does not twin, the contribution of twins to the tensile strain would be smaller and depends on the twin volume fraction: for example, for $f = 0.05$, the tensile strain would be ~1.2% (which is less than 3% of the total true strain of this specimen). Similar calculations can be performed for the other measured twin volume fractions and the results are plotted in Fig. 8b (vertical axis on the right) as a function of the true tensile strain. Overall, because the twin volume fractions are relatively low, their contributions to the total tensile strain are relatively small. However, there is another contribution of twinning to ductility. As discussed later, the new twin boundaries that form during straining ("dynamic Hall-Petch") play an important role in providing a source of steady strain hardening, which delays the onset of necking and enhances the achievable uniform elongation before fracture.

3.3. Evolution of dislocation density

A sequence of TEM BF micrographs showing the dislocation density evolution at 293 K and 77 K is presented in Fig. 9a–d and Fig. 9e–h, respectively. Note that all micrographs in Fig. 9 have the same magnification and the same contrast conditions, i.e., $\boldsymbol{g} = (111)$ as indicated by black arrows in the lower right corners of the micrographs. Similar true strain levels, shown in the upper left corner

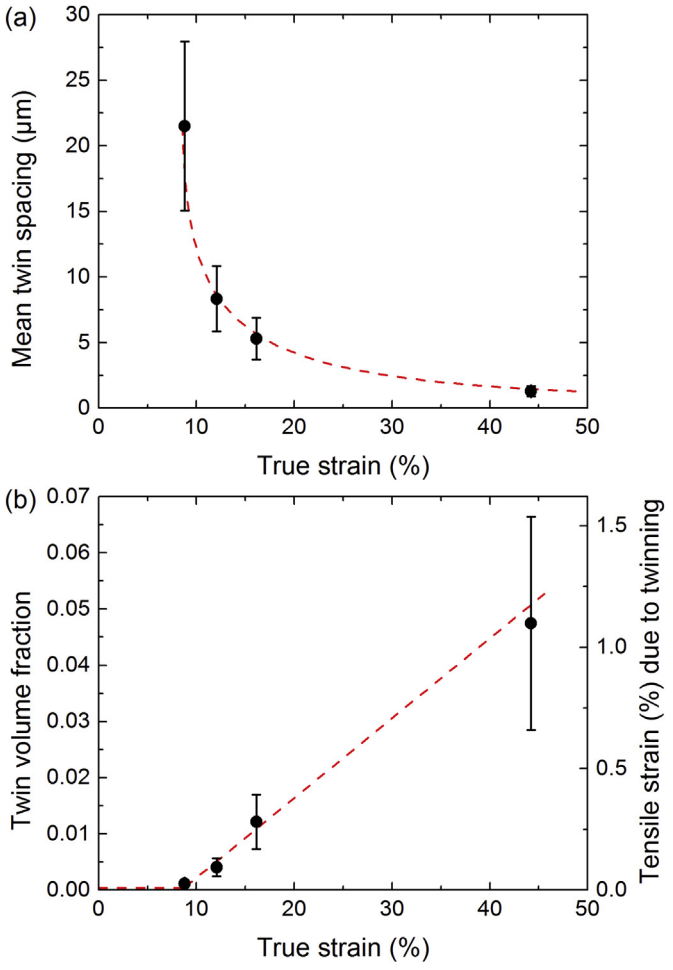

Fig. 8. (a) Mean twin spacing and (b) twin volume fraction and tensile strain due to twinning as a function of true plastic strain at 77 K.

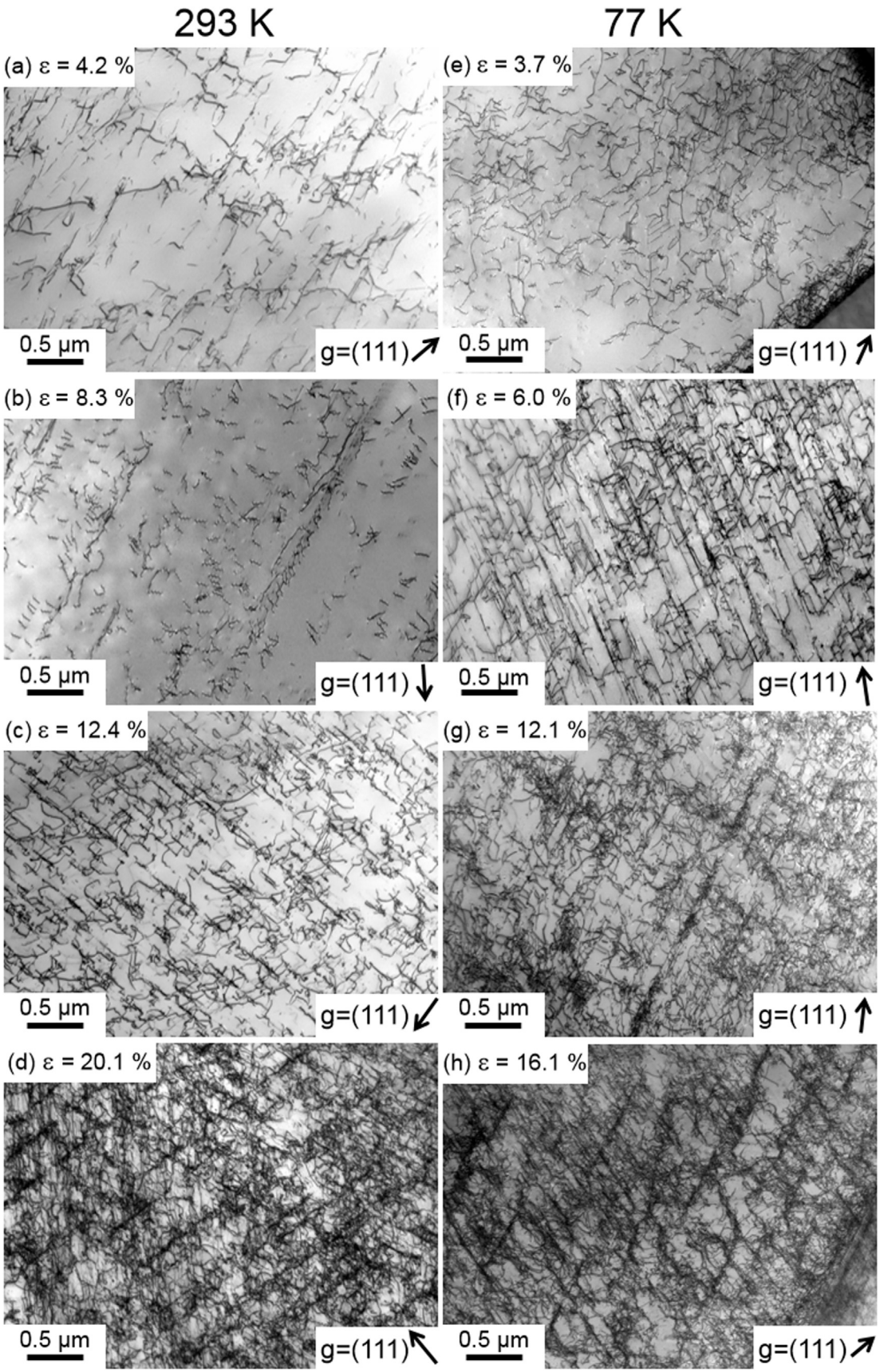

Fig. 9. TEM micrographs showing the evolution of dislocation structure with increasing true tensile strain at (a–d) 293 K and (e–h) 77 K.

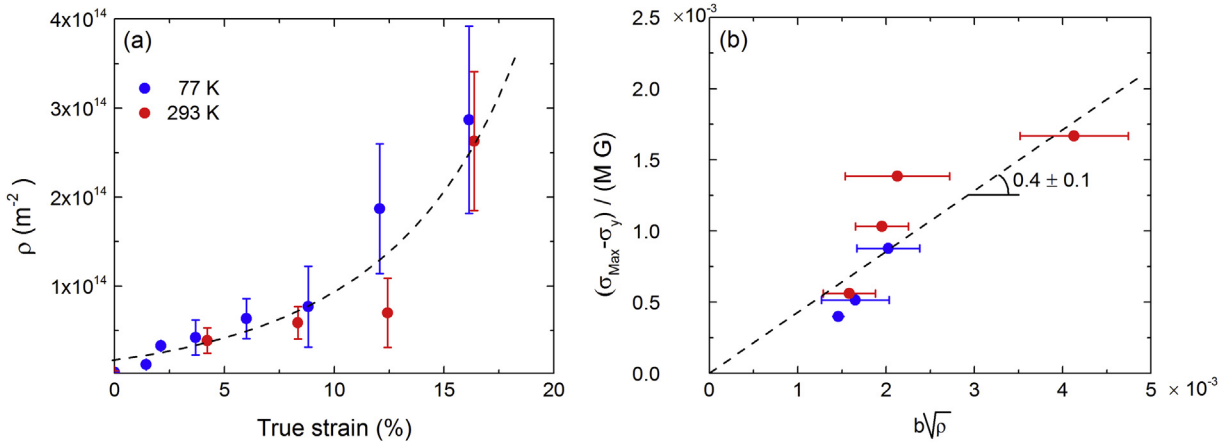

Fig. 10. (a) Dislocation density ρ as a function of true strain. (b) Taylor hardening plot showing linear dependence of the normalized work hardening $(\sigma_{Max} - \sigma_y)/(M\,G)$ as a function of $(b\,\rho^{1/2})$.

of each micrograph, were used to compare the dislocation microstructures at 293 K and 77 K. In the initial stages of tensile straining at both temperatures, the microstructural evolution is associated with the formation of dislocation pile-ups. Larger strains result in higher dislocation densities and eventually to their reorganization into cell structures around 20% strain.

Dislocation densities were measured after deformation at 293 K and 77 K up to 20% strain using TEM. Above 20% strain, the dislocation densities were too high to be accurately measured. Fig. 10a shows the change in dislocation density ρ as a function of strain where the error bars correspond to ±1 standard deviation of four measurements. Note that the magnitude of the error bars in Fig. 10a increases with strain due to the increased difficulty of measuring dislocation densities. Interestingly, the evolution of dislocation density is similar at 77 K and 293 K, which means that the early occurrence of mechanical twinning at 77 K (Fig. 4) has no significant effect on the subsequent evolution of dislocation density since the same dislocation density evolution is seen also at room temperature where twins form only in the final stage of deformation, close to fracture (Fig. 6). The temperature independent evolution of dislocation density is in good agreement with the fact that the work hardening rate of FCC metals at low strains has been reported to be relatively independent of temperature [48]. The main difference in the stress-strain curves at higher temperatures is that recovery processes such as cross-slip occur at an earlier stage, which results in a decrease of the work hardening rate at larger strains [48].

According to the Taylor hardening model, the increase in shear stress $(\Delta\tau)$ due to forest dislocation interactions is given by:

$$\Delta\tau = \Delta\sigma/\mathrm{M} = \alpha\,\mathrm{G}\,b\,\rho^{1/2} \qquad (2)$$

where $\Delta\sigma$ is the corresponding increase in the tensile stress, M is the Taylor factor (3.06), α is a constant, G is the shear modulus (85 and 80 GPa at 77 K and 293 K, respectively) [20,45], b is the magnitude of the Burgers vector (0.254 nm at 77 K and 0.255 nm at 293 K [20]), and ρ is the dislocation density. Therefore, if the modulus-normalized increment of stress, $(\sigma_{max} - \sigma_y)/M\,G$, is plotted as a function of $b\,\rho^{1/2}$, we should obtain a straight line, which is approximately what we find, as shown in Fig. 10b. Here σ_{max} is the maximum applied stress prior to unloading, σ_y is the yield stress, and only data from those specimens in which twinning was not observed are included. Despite some scatter, which has been remarked upon in the literature [49], the data points can be reasonably fitted to a straight line going through the origin with a slope $\alpha = 0.4 \pm 0.1$. This value is in reasonable agreement with that found for single crystals and polycrystals of copper using TEM ($\alpha = 0.5$) [50,51].

3.4. Dynamic Hall-Petch strengthening due to twinning

While the physical nature and magnitude of strengthening due to twinning is still a subject of debate, it is generally accepted that twinning during straining progressively introduces new interfaces that reduce the dislocation mean free path and cause strengthening [33,52–55]. This is commonly referred to as the "dynamic Hall–Petch" effect. In addition, Idrissi et al. [56–59] reported that mechanical twins contain a high density of sessile dislocations that act as strong barriers to dislocation glide, which further contributes to strain hardening. In the present HEA, the effect of twinning on strain hardening can be understood by revisiting Fig. 2c, where the strain hardening rates at 77 K and 293 K are identical up to strains of ~7%. Beyond that, the two curves diverge: the 77 K curve becomes flat indicating steady (continuous) work hardening whereas the strain hardening rate at 293 K shows a monotonic decrease. A comparison of Fig. 2c with Fig. 4 shows that, the strain at which the 77 K curve becomes flat is roughly the point at which twinning sets in. Were it not for this, the deformation would be accommodated fully by dislocation plasticity, as is the case at 293 K where twinning is seen only after very high strains close to the fracture strain. At both temperatures, the evolution of dislocation density with strain is similar (Fig. 10a), as is the contribution of dislocations to the modulus-normalized strain hardening (Fig. 10b). Therefore, in the absence of twinning, the 77-K curve in Fig. 2c would follow the same trajectory as the 293-K curve. Our present results clearly show that dislocation hardening by itself is not capable of providing the necessary work hardening rate and twinning is needed to explain the increased strength-ductility combination as the temperature is decreased from room temperature down to liquid nitrogen temperature.

To quantify the contribution of mechanical twinning to the flow stress, additional tensile specimens were first pre-strained to various amounts at 77 K, unloaded, and then tensile tested at 293 K. Fig. 11 shows selected true stress-strain curves (in blue) of four different specimens that were pre-strained at 77 K to 5.7, 13.4, 29.2, 38.4% true strain and unloaded. After these pre-strains, the individual specimens were tensile tested to fracture at 293 K (green curves). For comparison, the stress-strain behavior of specimens that were directly tensile tested at 293 K, without any

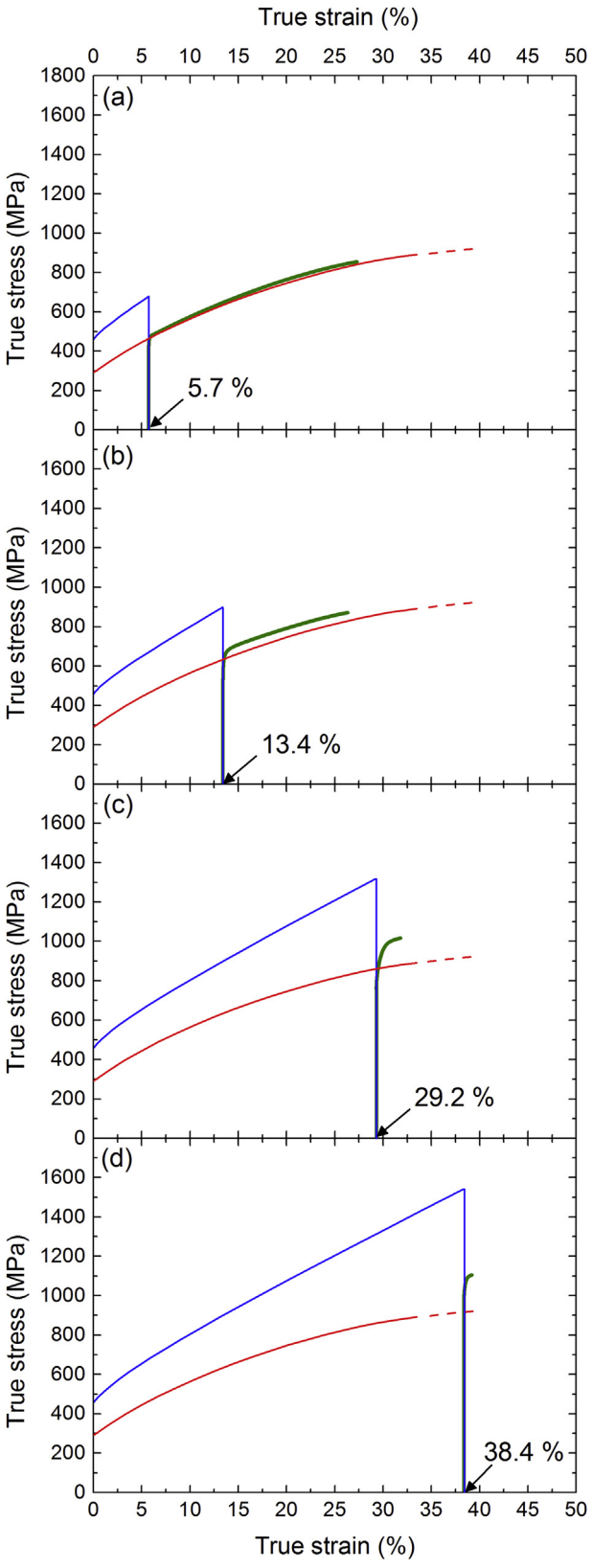

Fig. 11. Effect of various amounts of tensile pre-strain at 77 K (blue curves) on subsequent stress-strain behavior at 293 K (green curves). For comparison, the red curves show the stress-strain behavior of a specimen directly strained to fracture at 293 K, i.e., without any pre-strain at 77 K. The red dashed lines are extrapolations beyond the fracture strain. (For interpretation of the references to color in this figure legend, the reader is referred to the web version of this article.)

pre-strain at 77 K, are shown by the red curves (the dashed portions of these curves are hypothetical extrapolations beyond fracture). After a pre-strain of 5.7% at 77 K (Fig. 11a), the subsequent stress-strain curve at room temperature is almost identical to that of the specimen that was not pre-strained. This suggests that the microstructural evolution is similar at 77 K and 293 K, consistent with our TEM observations which showed that for strains below ~7.4% there is only dislocation plasticity and the dislocation density increases similarly at the two temperatures (Fig. 10a). Since flow stress depends only on dislocation density, whose evolution is the same at the two temperatures, there is no discernable effect of pre-straining at liquid nitrogen temperature on the subsequent tensile behavior at room temperature (consistent with the Cottrell-Stokes law, [60]). However, for larger pre-strains at 77 K (Fig. 11b–d), mechanical twinning sets in and this increases the subsequent flow stress at room temperature. The stress increment due to twinning increases with increasing pre-strain at 77 K, probably because the twin volume fraction increases (Fig. 8b). Significantly, the twins introduced during the pre-strain at 77 K increase the ductility at 293 K, as can be seen in Fig. 11d from the extra elongations of the green curve in the region of the extrapolated red dashed line (where the specimens would normally have fractured had they not been pre-strained).

4. Conclusion

The tensile properties and microstructures of the CrMnFeCoNi HEA were investigated at liquid nitrogen temperature (77 K) and room temperature (293 K) and the following results were obtained.

1. At 77 K, deformation occurs by dislocation plasticity up to ~7.4% true strain beyond which twinning is activated as an additional deformation mode. The true tensile stress and resolved shear stress at which twinning occurs are 720 ± 30 MPa and 235 ± 10 MPa, respectively. The twinning shear makes a relatively small contribution to the total tensile strain because of the relatively low volume fraction of twins. However, it contributes significantly to strain hardening because of the extra boundaries introduced during twinning ("dynamic Hall-Petch").
2. At 293 K, deformation occurs by dislocation plasticity up to much higher true strains (>20%) and twinning is activated only close to the fracture strain. This is because of the much lower yield strength at 293 K as a result of which higher strains are required to reach the twinning stress by work hardening. At room temperature, twinning was not observed in a specimen subjected to a tensile stress of 680 MPa but was observed in a specimen subjected to a stress of 820 MPa, indicating that the twinning stress at 293 K is similar to that at 77 K (~720 MPa). This suggests that there is a "critical" resolved shear stress for twinning that is roughly the same at 293 K and 77 K (around 235 MPa).
3. The shear modulus normalized work hardening behaviors at 77 K and 293 K are similar up to ~7.4% true strain. In this strain range, work hardening is governed by the planar glide of dislocations whose densities increase with strain at a similar rate at the two temperatures.
4. Above ~7.4% true strain, the modulus normalized work hardening rate continues to decrease at 293 K while it remains constant at a very high value of $G/30$ at 77 K. The onset of twinning at 77 K coincides with this divergence of work hardening rates. Therefore, the enhanced strength-ductility combination at 77 K compared to 293 K is a direct result of twinning occurring earlier in the deformation process and postponing the onset of necking. Consistent with this, twins introduced by pre-

straining at 77 K increased the strength and ductility of specimens subsequently tensile tested at 293 K compared to those that were not pre-strained.

Acknowledgments

Funding from the German Research Foundation (DFG) is acknowledged through projects LA 3607/1-1 (G.L.), GE 2736/1-1 (E.P.G.), and project B7 of SFB/TR 103 (G.E.).

References

[1] B. Cantor, I.T.H. Chang, P. Knight, A.J.B. Vincent, Microstructural development in equiatomic multicomponent alloys, Mater. Sci. Eng. A 375–377 (2004) 213.
[2] F. Otto, Y. Yang, H. Bei, E.P. George, Relative effects of enthalpy and entropy on the phase stability of equiatomic high-entropy alloys, Acta Mater. 61 (2013) 2628.
[3] A. Gali, E.P. George, Tensile properties of high- and medium-entropy alloys, Intermetallics 39 (2013) 74.
[4] F. Otto, A. Dlouhý, C. Somsen, H. Bei, G. Eggeler, E.P. George, The influences of temperature and microstructure on the tensile properties of a CoCrFeMnNi high-entropy alloy, Acta Mater. 61 (2013) 5743.
[5] C. Zhu, Z.P. Lu, T.G. Nieh, Incipient plasticity and dislocation nucleation of FeCoCrNiMn high-entropy alloy, Acta Mater. 61 (2013) 2993.
[6] K.Y. Tsai, M.H. Tsai, J.W. Yeh, Sluggish diffusion in Co–Cr–Fe–Mn–Ni high-entropy alloys, Acta Mater. 61 (2013) 4887.
[7] A.J. Zaddach, C. Niu, C.C. Koch, D.L. Irving, Mechanical properties and stacking fault energies of NiFeCrCoMn High-entropy alloy, J. Miner. Metals Mater. Soc. (TMS) 65 (2013) 1780.
[8] W.H. Liu, Y. Wu, J.Y. He, T.G. Nieh, Z.P. Lu, Grain growth and the Hall–Petch relationship in a high-entropy FeCrNiCoMn alloy, Scr. Mater. 68 (2013) 526.
[9] J.Y. He, C. Zhu, D.Q. Zhou, W.H. Liu, T.G. Nieh, Z.P. Lu, Steady state flow of the FeCoNiCrMn high entropy alloy at elevated temperatures, Intermetallics 55 (2014) 9.
[10] P.P. Bhattacharjee, G.D. Sathiaraj, M. Zaid, J.R. Gatti, C. Lee, C.-W. Tsai, J.-W. Yeh, Microstructure and texture evolution during annealing of equiatomic CoCrFeMnNi high-entropy alloy, J. Alloys Compd. 587 (2014) 544.
[11] G.A. Salishchev, M.A. Tikhonovsky, D.G. Shaysultanov, N.D. Stepanov, A.V. Kuznetsov, I.V. Kolodiy, A.S. Tortika, O.N. Senkov, Effect of Mn and V on structure and mechanical properties of high-entropy alloys based on CoCrFeNi system, J. Alloys Compd. 591 (2014) 11.
[12] F. Otto, N.L. Hanold, E.P. George, Microstructural evolution after thermomechanical processing in an equiatomic, single-phase CoCrFeMnNi high-entropy alloy with special focus on twin boundaries, Intermetallics 54 (2014) 39.
[13] B. Gludovatz, A. Hohenwarter, D. Catoor, E.H. Chang, E.P. George, R.O. Ritchie, A fracture-resistant high-entropy alloy for cryogenic applications, Science 345 (2014) 1153.
[14] E.W. Huang, D. Yu, J.-W. Yeh, C. Lee, K. An, S.-Y. Tu, A study of lattice elasticity from low entropy metals to medium and high entropy alloys, Scr. Mater. 101 (2015) 32.
[15] W. Woo, E.W. Huang, J.-W. Yeh, H. Choo, C. Lee, S.-Y. Tu, In-situ neutron diffraction studies on high-temperature deformation behavior in a CoCrFeMnNi high entropy alloy, Intermetallics 62 (2015) 1.
[16] D. Ma, M. Yao, K.G. Pradeep, C.C. Tasan, H. Springer, D. Raabe, Phase stability of non-equiatomic CoCrFeMnNi high entropy alloys, Acta Mater. 98 (2015) 288.
[17] M. Laurent-Brocq, A. Akhatova, L. Perrière, S. Chebini, X. Sauvage, E. Leroy, Y. Champion, Insights into the phase diagram of the CrMnFeCoNi high entropy alloy, Acta Mater. 88 (2015) 355.
[18] G.D. Sathiaraj, P.P. Bhattacharjee, Effect of starting grain size on the evolution of microstructure and texture during thermo-mechanical processing of CoCrFeMnNi high entropy alloy, J. Alloys Compd. 647 (2015) 82.
[19] S. Huang, W. Li, S. Lu, F. Tian, J. Shen, E. Holmström, L. Vitos, Temperature dependent stacking fault energy of FeCrCoNiMn high entropy alloy, Scr. Mater. 108 (2015) 44.
[20] G. Laplanche, P. Gadaud, O. Horst, F. Otto, G. Eggeler, E.P. George, Temperature dependencies of the elastic moduli and thermal expansion coefficient of an equiatomic, single-phase CoCrFeMnNi high-entropy alloy, J. Alloys Compd. 623 (2015) 348.
[21] G. Laplanche, O. Horst, F. Otto, G. Eggeler, E.P. George, Microstructural evolution of a CoCrFeMnNi high-entropy alloy after swaging and annealing, J. Alloys Compd. 647 (2015) 548.
[22] B. Schuh, F. Mendez-Martin, B. Völker, E.P. George, H. Clemens, R. Pippan, A. Hohenwarter, Mechanical properties, microstructure and thermal stability of a nanocrystalline CoCrFeMnNi high-entropy alloy after severe plastic deformation, Acta Mater. 96 (2015) 258.
[23] Z. Zhang, M.M. Mao, J. Wang, B. Gludovatz, Z. Zhang, S.X. Mao, E.P. George, Q. Yu, R.O. Ritchie, Nanoscale origins of the damage tolerance of the high-entropy alloy CrMnFeCoNi, Nat. Commun. (2015) 6.
[24] B. Gludovatz, E.P. George, R.O. Ritchie, Processing, microstructure and mechanical properties of the CrMnFeCoNi high-entropy alloy, J. Miner. Metals Mater. Soc. (TMS) 67 (2015) 2262.
[25] L. Patriarca, A. Ojha, H. Sehitoglu, Y.I. Chumlyakov, Slip nucleation in single crystal FeNiCoCrMn high entropy alloy, Scr. Mater. 112 (2016) 54.
[26] E.J. Pickering, R. Muñoz-Moreno, H.J. Stone, N.G. Jones, Precipitation in the equiatomic high-entropy alloy CrMnFeCoNi, Scr. Mater. 113 (2016) 106.
[27] T.M. Smith, M.S. Hooshmand, B.D. Esser, F. Otto, D.W. McComb, E.P. George, M. Ghazisaeidi, M.J. Mills, Atomic-scale characterization and modeling of 60° dislocations in a high-entropy alloy, Acta Mater. 110 (2016) 352.
[28] G. Laplanche, U.F. Volkert, G. Eggeler, E.P. George, Oxidation behavior of the CrMnFeCoNi high-entropy alloy, Oxid. Metals 85 (2016) 629.
[29] F. Otto, A. Dlouhý, K.G. Pradeep, M. Kubĕnová, D. Raabe, G. Eggeler, E.P. George, Decomposition of the single-phase high-entropy alloy CrMnFeCoNi after prolonged anneals at intermediate temperatures, Acta Mater. 112 (2016) 40.
[30] N. Stepanov, M. Tikhonovsky, N. Yurchenko, D. Zyabkin, M. Klimova, S. Zherebtsov, A. Efimov, G. Salishchev, Effect of cryo-deformation on structure and properties of CoCrFeNiMn high-entropy alloy, Intermetallics 59 (2015) 8.
[31] E.J. Pickering, N.G. Jones, High-entropy alloys: a critical assessment of their founding principles and future prospects, Int. Mater. Rev. 61 (2016) 183.
[32] Z. Wu, C.M. Parish, H. Bei, Nano-twin mediated plasticity in carbon-containing FeNiCoCrMn high entropy alloys, J. Alloys Compd. 647 (2015) 815.
[33] L. Remy, Kinetics of f.c.c. deformation twinning and its relationship to stress-strain behaviour, Acta Metall. 26 (1978) 443.
[34] E. El-Danaf, S.R. Kalidindi, R.D. Doherty, Influence of grain size and stacking-fault energy on deformation twinning in fcc metals, Metall. Mater. Trans. A 30 (1999) 1223.
[35] K. Jeong, J.-E. Jin, Y.-S. Jung, S. Kang, Y.-K. Lee, The effects of Si on the mechanical twinning and strain hardening of Fe–18Mn–0.6C twinning-induced plasticity steel, Acta Mater. 61 (2013) 3399.
[36] I. Gutierrez-Urrutia, D. Raabe, Dislocation and twin substructure evolution during strain hardening of an Fe–22 wt.% Mn–0.6 wt.% C TWIP steel observed by electron channeling contrast imaging, Acta Mater. 59 (2011) 6449.
[37] D.R. Steinmetz, T. Jäpel, B. Wietbrock, P. Eisenlohr, I. Gutierrez-Urrutia, A. Saeed–Akbari, T. Hickel, F. Roters, D. Raabe, Revealing the strain-hardening behavior of twinning-induced plasticity steels: theory, simulations, experiments, Acta Mater. 61 (2013) 494.
[38] Y.S. Li, N.R. Tao, K. Lu, Microstructural evolution and nanostructure formation in copper during dynamic plastic deformation at cryogenic temperatures, Acta Mater. 56 (2008) 230.
[39] R.K. Ham, The determination of dislocation densities in thin films, Philos. Mag. 6 (1961) 1183.
[40] P.M. Kelly, A. Jostsons, R.G. Blake, J.G. Napier, The determination of foil thickness by scanning transmission electron microscopy, Phys. Status Solidi (a) 31 (1975) 771.
[41] S.M. Allen, Foil thickness measurements from convergent-beam diffraction patterns, Philos. Mag. A 43 (1981) 325.
[42] D.B. Williams, C.B. Carter, Transmission Electron Microscopy: a Textbook for Materials Science, Springer US, Boston, MA, 1996.
[43] M.A. Meyers, A. Mishra, D.J. Benson, Mechanical properties of nanocrystalline materials, Prog. Mater. Sci. 51 (2006) 427.
[44] H. Bahmanpour, K.M. Youssef, J. Horky, D. Setman, M.A. Atwater, M.J. Zehetbauer, R.O. Scattergood, C.C. Koch, Deformation twins and related softening behavior in nanocrystalline Cu–30% Zn alloy, Acta Mater. 60 (2012) 3340.
[45] A. Haglund, M. Koehler, D. Catoor, E.P. George, V. Keppens, Polycrystalline elastic moduli of a high-entropy alloy at cryogenic temperatures, Intermetallics 58 (2015) 62.
[46] M.A. Meyers, O. Vöhringer, V.A. Lubarda, The onset of twinning in metals: a constitutive description, Acta Mater. 49 (2001) 4025.
[47] R.L. Fullman, Measurement of approximately cylindrical particles in opaque samples, Trans. Metall. Soc. AIME 197 (1953) 447.
[48] R.W.K. Honeycombe, The Plastic Deformation of Metals, second ed., Edward Arnold Ltd, London, 1984.
[49] J.A. Venables, Dislocation distributions and densities in F.C.C. copper alloys, Philos. Mag. 7 (1962) 1969.
[50] J.E. Bailey, The dislocation density, flow stress and stored energy in deformed polycrystalline copper, Philos. Mag. 8 (1963) 223.
[51] H. Mecking, U.F. Kocks, Kinetics of flow and strain-hardening, Acta Metall. 29 (1981) 1865.
[52] S. Mahajan, D.F. Williams, Deformation twinning in metals and alloys, Int. Metall. Rev. 18 (1973) 43.
[53] J.W. Christian, S. Mahajan, Deformation twinning, Prog. Mater. Sci. 39 (1995) 1.
[54] O. Bouaziz, S. Allain, C. Scott, Effect of grain and twin boundaries on the hardening mechanisms of twinning-induced plasticity steels, Scr. Mater. 58 (2008) 484.
[55] O. Bouaziz, S. Allain, Y. Estrin, Effect of pre-strain at elevated temperature on strain hardening of twinning-induced plasticity steels, Scr. Mater. 62 (2010) 713.
[56] H. Idrissi, L. Ryelandt, M. Veron, D. Schryvers, P.J. Jacques, Is there a relationship between the stacking fault character and the activated mode of plasticity of Fe–Mn-based austenitic steels? Scr. Mater. 60 (2009) 941.
[57] H. Idrissi, K. Renard, D. Schryvers, P.J. Jacques, On the relationship between the twin internal structure and the work-hardening rate of TWIP steels, Scr.

Mater. 63 (2010) 961.
[58] H. Idrissi, K. Renard, L. Ryelandt, D. Schryvers, P.J. Jacques, On the mechanism of twin formation in Fe–Mn–C TWIP steels, Acta Mater. 58 (2010) 2464.
[59] K. Renard, H. Idrissi, D. Schryvers, P.J. Jacques, On the stress state dependence of the twinning rate and work hardening in twinning-induced plasticity steels, Scr. Mater. 66 (2012) 966.
[60] A.H. Cottrell, R.J. Stokes, Effects of temperature on the plastic properties of aluminium crystals, Proc. R. Soc. Lond. A Math. Phys. Eng. Sci. 233 (1955) 17.